Available online at www.sciencedirect.com
ScienceDirect
Applied Numerical Mathematics 57 (2007) 920–938
APPLIED NUMERICAL MATHEMATICS
www.elsevier.com/locate/apnum

# On a solenoidal Fourier–Chebyshev spectral method for stability analysis of the Hagen–Poiseuille flow ☆

A. Meseguer *, F. Mellibovsky

*Departament de Fisica Aplicada, Univ. Politècnica de Catalunya, C/Jordi Girona 1-3, Mod. B5, 08034 Barcelona, Spain*

---

**Abstract**

In this work we study the efficiency of a spectral Petrov–Galerkin method for the linear and nonlinear stability analysis of the pipe or Hagen–Poiseuille flow. We formulate the problem in solenoidal primitive variables for the velocity field and the pressure term is eliminated from the scheme suitably projecting the equations on another solenoidal subspace. The method is unusual in being based on Chebyshev polynomials of selected parity for the radial variable, avoiding clustering of the quadrature points near the origin, satisfying appropriate regularity conditions at the pole and allowing the use of a fast cosine transform if required. Besides, this procedure provides good conditions for the time marching schemes. For the time evolution, we use semi-implicit time integration schemes. Special attention is given to the explicit treatment and efficient evaluation of the nonlinear terms via pseudospectral partial summations. The method provides spectral accuracy and the linear and nonlinear results obtained are in very good agreement with previous works. The scheme presented can be applied to other flows in unbounded cylindrical geometries.

*Keywords:* Solenoidal spectral methods; Navier–Stokes equations; Pipe flows

---

## 1. Introduction

Spectral methods have been extensively applied for the approximation of solutions of the Navier–Stokes equations [3,4,8]. So far, collocation or pseudospectral methods have been more popular than Galerkin spectral because they are easier to formulate and implement. One of the arguments that have been frequently given to encourage the use of Galerkin instead of collocation methods is that sometimes the former provide banded matrices in the spatial discretization of linear operators, which improves the efficiency of the linear solvers in the time integrations. The difficulty of Galerkin methods lies on their mathematical formulation. In particular, the Navier–Stokes equations in non-Cartesian geometries make the Galerkin formulation very complex and tedious.

The numerical approximation of pipe flows via spectral or pseudospectral methods is not a new matter. There has been a long list of contributions regarding this issue in the recent past. Among other works, we should mention the methods proposed in [2,11,13,14,19,20,24], for example. In [14], a solenoidal Fourier–Jacobi spectral method was

---

☆ This work was supported by the Spanish Ministry of Science and Technology, grant FIS2004-01336 and also by the Engineering and Physical Sciences Research Council of the United Kingdom, under postdoctoral grant No. GR/M30890. The first author thanks Nick Trefethen for the supervision of part of the present work, carried out at Oxford University.

* Corresponding author.
*E-mail address:* alvar@fa.upc.edu (A. Meseguer).

0168-9274/$30.00 © 2006 IMACS. Published by Elsevier B.V. All rights reserved.
doi:10.1016/j.apnum.2006.09.002

proposed, elegantly solving the problem of the apparent singularity at the origin since the Jacobi polynomials used in the radial coordinate automatically satisfied the suitable analyticity conditions at the pole. Besides, the pressure terms were eliminated from the formulation via projection over a solenoidal space of test functions. The only weakness of the method proposed in [14] was the lack of a fast transform for the Jacobi polynomials and the clustering of radial points near the axis, thus considerably reducing the time step size in the time integrations. In a recent work [20], a Fourier–Chebyshev collocation method was formulated in primitive velocity-pressure variables, where Chebyshev polynomials of selected parity combined with half radial Gauss–Lobatto grid were used, thus avoiding clustering near the origin and allowing the use of a fast cosine transform. To the author's knowledge, this is the first time where the combination proposed in [20] has been used in Navier–Stokes equations in cylindrical coordinates.

In [18], a spectral solenoidal Petrov–Galerkin scheme was used for the accurate computation of eigenvalues arising from the linearization of the Navier–Stokes operator of the Hagen–Poiseuille flow. The analysis presented was focused on the asymptotic behaviour of the leading eigenvalues but the technical details of the spatial discretization and its efficiency for nonlinear time dependent integrations had to wait until a complete nonlinear formulation of the scheme was provided and tested.

In this work, a Galerkin method capable of simultaneously dealing with several difficulties arising from the Navier–Stokes equations in cylindrical unbounded geometries is presented. First, the construction of a solenoidal basis of trial functions for the velocity field in order to satisfy the incompressibility condition identically. In addition, this basis has to satisfy suitable physical boundary conditions at the pipe wall and also be analytic in a neighbourhood of the apparent singularity located at the origin in order to provide spectral accuracy. Second, the obtention of a dual basis of solenoidal test functions so that the pressure terms cancel out from the scheme once the projection has been carried out. The result of that projection should lead to inner products involving orthogonal or almost-orthogonal functions so the resulting discretized operators are banded matrices. Third, devising an optimal quadrature rule in the radial variable capable of avoiding clustering of points near the center axis and allowing a fast transform in that variable if possible. Avoiding clustering near the pole should also improve the time step restrictions due to the CFL conditions. Fourth, developing a pseudospectral algorithm for the efficient computation of the nonlinear terms via partial summation techniques. Finally, the implementation of the described discretization within a robust time marching scheme capable of overcoming the difficulties arising from the stiffness of the resulting systems of ODE.

The paper is structured as follows. In Section 2, the nonlinear initial-boundary stability problem is formulated mathematically. Section 3 is devoted to the detailed formulation of the trial and test solenoidal functions, focusing on their analyticity and radial symmetry properties. Section 4 describes the projection procedure that leads to the weak formulation of the problem as a dynamical system of amplitudes. In Section 5, an analysis of the linear stability of the basic Hagen–Poiseuille flow is presented, mainly focused on detailed explorations regarding the structure of the eigenmodes, providing accurate numerical tables of eigenvalues to be compared with other spectral schemes. The time marching algorithm and the efficient computation of the nonlinear terms via pseudospectral collocation and partial summation techniques are explained in Section 6. The validation of the numerical algorithm for unsteady computations is provided in Section 7 based on a comparison with previous works and on a comparative performance analysis between two linearly implicit methods. Finally, Section 8 is devoted to the numerical simulation of a particular transition to turbulence scenario in pipe flow.

## 2. Formulation of the problem

We consider the motion of an incompressible viscous fluid of kinematic viscosity $\nu$ and density $\rho$. The fluid is driven through a circular pipe of radius $a$ and infinite length by a uniform pressure gradient, $\Pi_0$, parallel to the axis of the pipe. We formulate the problem in cylindrical coordinates. The velocity of the fluid is prescribed by its radial ($\hat{\boldsymbol{r}}$), azimuthal ($\hat{\boldsymbol{\theta}}$) and axial ($\hat{\boldsymbol{z}}$) components

$$\mathbf{v} = u\hat{\boldsymbol{r}} + v\hat{\boldsymbol{\theta}} + w\hat{\boldsymbol{z}} = (u, v, w), \tag{1}$$

where $u$, $v$ and $w$ depend on the three spatial coordinates $(r, \theta, z)$ and time $t$. The motion of the fluid is governed by the incompressible Navier–Stokes equations

$$\partial_t \mathbf{v} + (\mathbf{v}\cdot\nabla)\mathbf{v} = -\frac{\Pi_0}{\rho}\hat{\boldsymbol{z}} - \nabla p + \nu\Delta\mathbf{v}, \tag{2}$$

$$\nabla\cdot\mathbf{v} = 0, \tag{3}$$

where $\mathbf{v}$ is the velocity vector field, satisfying the no-slip boundary condition at the wall,

$$\mathbf{v}_{\text{pipe wall}} = \mathbf{0}, \tag{4}$$

and $p$ is the reduced pressure. A basic steady solution of (2), (3) and (4) is the so-called *Hagen–Poiseuille flow*

$$\mathbf{v}_{\mathrm{B}} = (u_{\mathrm{B}}, v_{\mathrm{B}}, w_{\mathrm{B}}) = \left(0, 0, -\frac{\Pi_0 a^2}{4\rho\nu}\left[1 - \left(\frac{r}{a}\right)^2\right]\right), \qquad p_{\mathrm{B}} = \mathrm{C}, \tag{5}$$

where $\mathrm{C}$ is an arbitrary constant. This basic flow is a parabolic axial velocity profile which only depends on the radial coordinate [1]. The velocity of the fluid attains a maximum value $U_{\mathrm{CL}} = -\Pi_0 a^2/4\rho\nu$ at the center-line or axis of the cylinder.

Henceforth, all variables will be rendered dimensionless using $a$ and $U_{\mathrm{CL}}$ as space and velocity units, respectively. The axial coordinate $z$ is unbounded since the length of the pipe is infinite. In what follows, we assume that the flow is axially periodic with period $b$. In the dimensionless system, the spatial domain $\Omega$ of the problem is

$$\Omega = \{(r, \theta, z) \mid 0 \leqslant r \leqslant 1,\ 0 \leqslant \theta < 2\pi,\ 0 \leqslant z < Q\}, \tag{6}$$

where $Q = b/a$ is the dimensionless length of the pipe, in radii units. In the new variables, the basic flow takes the form

$$\mathbf{v}_{\mathrm{B}} = (u_{\mathrm{B}}, v_{\mathrm{B}}, w_{\mathrm{B}}) = (0, 0, 1 - r^2). \tag{7}$$

Finally, the parameter which governs the dynamics of the problem is the *Reynolds number*

$$Re = \frac{aU_{\mathrm{CL}}}{\nu}. \tag{8}$$

For the stability analysis, we suppose that the basic flow is perturbed by a solenoidal velocity field vanishing at the pipe wall

$$\mathbf{v}(r, \theta, z, t) = \mathbf{v}_{\mathrm{B}}(r) + \mathbf{u}(r, \theta, z, t), \qquad \nabla \cdot \mathbf{u} = 0, \qquad \mathbf{u}(r = 1) = \mathbf{0}, \tag{9}$$

and a perturbation pressure field

$$p(r, \theta, z, t) = p_{\mathrm{B}}(z) + q(r, \theta, z, t). \tag{10}$$

On introducing the perturbed fields in the Navier–Stokes equations, we obtain a nonlinear initial-boundary problem for the perturbations $\mathbf{u}$ and $q$:

$$\partial_t \mathbf{u} = -\nabla q + \frac{1}{Re}\Delta\mathbf{u} - (\mathbf{v}_{\mathrm{B}} \cdot \nabla)\mathbf{u} - (\mathbf{u} \cdot \nabla)\mathbf{v}_{\mathrm{B}} - (\mathbf{u} \cdot \nabla)\mathbf{u}, \tag{11}$$

$$\nabla \cdot \mathbf{u} = 0, \tag{12}$$

$$\mathbf{u}(1, \theta, z, t) = 0, \tag{13}$$

$$\mathbf{u}(r, \theta + 2\pi n, z, t) = \mathbf{u}(r, \theta, z, t), \tag{14}$$

$$\mathbf{u}(r, \theta, z + lQ, t) = \mathbf{u}(r, \theta, z, t), \tag{15}$$

$$\mathbf{u}(r, \theta, z, 0) = \mathbf{u}_0, \qquad \nabla \cdot \mathbf{u}_0 = 0, \tag{16}$$

for $(n, l) \in \mathbb{Z}^2$, $(r, \theta, z) \in [0, 1] \times [0, 2\pi) \times [0, Q)$ and $t > 0$. Eq. (11) describes the nonlinear space-time evolution of the perturbation of the velocity field. Eq. (12) is the solenoidal condition for the perturbation, and Eqs. (13)–(15) describe the homogeneous boundary condition for the radial coordinate and the periodic boundary conditions for the azimuthal and axial coordinates respectively. Finally, Eq. (16) is the initial solenoidal condition for the perturbation field at $t = 0$.

## 3. Trial and test solenoidal bases

This section will deal with the generation of solenoidal bases for our approximation of the vector field $\mathbf{u}$ appearing in (9). We discretize the perturbation $\mathbf{u}$ by a spectral approximation $\mathbf{u}_{\mathrm{S}}$ of order $L$ in $z$, order $N$ in $\theta$, and order $M$ in $r$,

$$\mathbf{u}_{\mathrm{S}}(r, \theta, z, t) = \sum_{l=-L}^{L} \sum_{n=-N}^{N} \sum_{m=0}^{M} a_{lnm}(t)\boldsymbol{\Phi}_{lnm}(r, \theta, z), \tag{17}$$

where $\boldsymbol{\Phi}_{lnm}$ are *trial* bases of solenoidal vector fields of the form

$$\boldsymbol{\Phi}_{lnm}(r,\theta,z)=\mathrm{e}^{\mathrm{i}(2\pi lz/Q+n\theta)}\mathbf{v}_{lnm}(r), \tag{18}$$

satisfying

$$\nabla\cdot\boldsymbol{\Phi}_{lnm}=0 \tag{19}$$

for $l=-L,\dots,L$, $n=-N,\dots,N$ and $m=0,\dots,M$. The trial bases (18) must satisfy certain regularity conditions at the origin, be periodic in the axial and azimuthal directions, and satisfy homogeneous boundary conditions at the wall,

$$\boldsymbol{\Phi}_{lnm}(1,\theta,z)=\mathbf{0}, \tag{20}$$

according to Eqs. (12)–(15).

There are many different ways of obtaining divergence-free fields in polar coordinates [14,17,15]. The solenoidal condition (19) can be written as

$$\left(\partial_r+\frac{1}{r}\right)u_{lnm}+\frac{\mathrm{i}n}{r}v_{lnm}+\mathrm{i}l\frac{2\pi}{Q}w_{lnm}=0, \tag{21}$$

where

$$\mathbf{v}_{lnm}=u_{lnm}\hat{\boldsymbol{r}}+v_{lnm}\hat{\boldsymbol{\theta}}+w_{lnm}\hat{\boldsymbol{z}}=(u_{lnm},v_{lnm},w_{lnm}). \tag{22}$$

Eq. (21) introduces a linear dependence between the three components of $\mathbf{v}_{lnm}$, leading to two degrees of freedom. In what follows, we define

$$\mathrm{h}_m(r)=\left(1-r^2\right)\mathrm{T}_{2m}(r),\qquad \mathrm{g}_m(r)=\left(1-r^2\right)\mathrm{h}_m(r),\qquad \mathrm{D}=\frac{\mathrm{d}}{\mathrm{d}r},\qquad \mathrm{D}_+=\mathrm{D}+\frac{1}{r},\qquad \mathrm{k}_0=\frac{2\pi}{Q}, \tag{23}$$

where $\mathrm{T}_{2m}(r)$ is the Chebyshev polynomial of degree $2m$ and $r\in[0,1]$, and $\mathrm{k}_0$ stands for the fundamental axial wavenumber in the axial coordinate. Following the regularization rules proposed in [20], we distinguish two cases:

I. *Axisymmetric fields* ($n=0$): The basis is spanned by the elements

$$\boldsymbol{\Phi}^{(1)}_{l0m}=\mathrm{e}^{\mathrm{i}\mathrm{k}_0lz}\mathbf{v}^{(1)}_{l0m}=\mathrm{e}^{\mathrm{i}\mathrm{k}_0lz}(0,r\mathrm{h}_m,0), \tag{24}$$

$$\boldsymbol{\Phi}^{(2)}_{l0m}=\mathrm{e}^{\mathrm{i}\mathrm{k}_0lz}\mathbf{v}^{(2)}_{l0m}=\mathrm{e}^{\mathrm{i}\mathrm{k}_0lz}\left(-\mathrm{i}\mathrm{k}_0lr\mathrm{g}_m,0,\mathrm{D}_+[r\mathrm{g}_m]\right), \tag{25}$$

except that if $l=0$, the third component of $\boldsymbol{\Phi}^{(2)}_{lnm}$ is replaced by $\mathrm{h}_m(r)$.

II. *Non-axisymmetric fields* ($n\neq 0$): In this case, the basis is spanned by the elements

$$\boldsymbol{\Phi}^{(1)}_{lnm}=\mathrm{e}^{\mathrm{i}(n\theta+\mathrm{k}_0lz)}\mathbf{v}^{(1)}_{lnm}=\mathrm{e}^{\mathrm{i}(n\theta+\mathrm{k}_0lz)}\left(-\mathrm{i}nr^{\sigma-1}\mathrm{g}_m,\mathrm{D}\left[r^{\sigma}\mathrm{g}_m\right],0\right), \tag{26}$$

$$\boldsymbol{\Phi}^{(2)}_{lnm}=\mathrm{e}^{\mathrm{i}(n\theta+\mathrm{k}_0lz)}\mathbf{v}^{(2)}_{lnm}=\mathrm{e}^{\mathrm{i}(n\theta+\mathrm{k}_0lz)}\left(0,-\mathrm{i}\mathrm{k}_0lr^{\sigma+1}\mathrm{h}_m,\mathrm{i}nr^{\sigma}\mathrm{h}_m\right), \tag{27}$$

where

$$\sigma=\begin{cases}2 & (n\text{ even}),\\ 1 & (n\text{ odd}).\end{cases} \tag{28}$$

The binomial factors $(1-r^2)$ and $(1-r^2)^2$ appearing in $\mathrm{h}_m(r)$ and $\mathrm{g}_m(r)$ are responsible for the boundary conditions (20) at the pipe wall to be satisfied. Factors of the form $1-r$ or $(1-r)^2$ would also solve the boundary problem, but they would violate the parity conditions established by Theorem 1 of [20]. The monomials $r$, $r^{\sigma}$ and $r^{\sigma\pm1}$ appearing in Eqs. (24)–(27) enforce the conditions of regularity and parity at the pole. The pure imaginary factors in $\boldsymbol{\Phi}^{(2)}_{lnm}$ could be dispensed with, but we leave them in so that the basis functions have a desirable symmetry property: if $l$ and $n$ are negated, each basis function is replaced by its complex conjugate, i.e.,

$$\left[\boldsymbol{\Phi}^{(1,2)}_{lnm}\right]^*=\boldsymbol{\Phi}^{(1,2)}_{-l,-n,m}. \tag{29}$$

The Galerkin scheme is accomplished when projecting the trial functions above described over a suitable dual or test space of vector fields. We consider the inner product $(\cdot,\cdot)$ as the volume integral over the domain of the pipe:

$$(\mathbf{a},\mathbf{b})=\int_0^Q\int_0^{2\pi}\int_0^1\mathbf{a}^*\cdot\mathbf{b}r\,\mathrm{d}r\,\mathrm{d}\theta\,\mathrm{d}z, \tag{30}$$

where $*$ stands for complex conjugate, **b** belongs to the physical or trial space and **a** is a solenoidal vector field belonging to the test or projection space still to be determined. We focus our attention on the radial integration involved in (30). Since the variable of the Chebyshev polynomials considered in the trial functions is the radius $r$, we need to relate that integral to an orthogonal product in the extended domain $r \in [-1, 1]$. A straightforward solution is to assume that

$$\int_0^1 \mathbf{a}^* \cdot \mathbf{b} r \,\mathrm{d}r = \frac{1}{2}\int_{-1}^1 \mathbf{a}^* \cdot \mathbf{b} r \,\mathrm{d}r. \tag{31}$$

The previous equation is only true if the integrand $\mathbf{a}^* \cdot \mathbf{b}r$ is an *even* function of the radius. This is the *crucial* point of the spectral projection in the radial variable. In order to satisfy Eq. (31), the test functions will consist of even Chebyshev polynomials $\mathrm{T}_{2m}(r)$, previously factorized with the Chebyshev weight $(1-r^2)^{-1/2}$ and suitable monomials $r^\beta$ so that the integrand becomes symmetric with respect to the center axis and the integrals can be computed exactly by using quadrature formulas.

For the test functions $\boldsymbol{\Psi}_{lnm}(r, \theta, z)$, we distinguish again two different situations:

I. *Axisymmetric fields* ($n = 0$): In this case, the basis is spanned by the elements

$$\boldsymbol{\Psi}^{(1)}_{l0m} = \mathrm{e}^{\mathrm{i}\mathrm{k}_0 l z}\tilde{\mathbf{v}}^{(1)}_{l0m}(r) = \frac{\mathrm{e}^{\mathrm{i}\mathrm{k}_0 l z}}{\sqrt{1-r^2}}(0, \mathrm{h}_m, 0), \tag{32}$$

$$\boldsymbol{\Psi}^{(2)}_{l0m} = \mathrm{e}^{\mathrm{i}\mathrm{k}_0 l z}\tilde{\mathbf{v}}^{(2)}_{l0m} = \frac{\mathrm{e}^{\mathrm{i}\mathrm{k}_0 l z}}{\sqrt{1-r^2}}\left(-\mathrm{k}_0\mathrm{i}lr^2\mathrm{g}_m, 0, \mathrm{D}_+\left[r^2\mathrm{g}_m\right] + r^3\mathrm{h}_m\right), \tag{33}$$

except that the third component of the vector in $\boldsymbol{\Psi}^{(2)}_{l0m}$ is replaced by $r\mathrm{h}_m(r)$ if $l = 0$.

II. *Non-axisymmetric fields* ($n \neq 0$): In this case, the basis is spanned by the elements

$$\boldsymbol{\Psi}^{(1)}_{lnm} = \mathrm{e}^{\mathrm{i}(n\theta+\mathrm{k}_0 l z)}\tilde{\mathbf{v}}^{(1)}_{lnm} = \frac{\mathrm{e}^{\mathrm{i}(n\theta+\mathrm{k}_0 l z)}}{\sqrt{1-r^2}}\left(\mathrm{i}nr^\beta\mathrm{g}_m, \mathrm{D}\left[r^{\beta+1}\mathrm{g}_m\right] + r^{\beta+2}\mathrm{h}_m, 0\right), \tag{34}$$

$$\boldsymbol{\Psi}^{(2)}_{lnm} = \mathrm{e}^{\mathrm{i}(n\theta+\mathrm{k}_0 l z)}\tilde{\mathbf{v}}^{(2)}_{lnm} = \frac{\mathrm{e}^{\mathrm{i}(n\theta+\mathrm{k}_0 l z)}}{\sqrt{1-r^2}}\left(0, -\mathrm{k}_0\mathrm{i}lr^{\beta+2}\mathrm{h}_m, \mathrm{i}nr^{\beta+1}\mathrm{h}_m\right), \tag{35}$$

except that the third component of the vector in $\boldsymbol{\Psi}^{(2)}_{lnm}$ is replaced by $r^{1-\beta}\mathrm{h}_m(r)$ if $l = 0$, where

$$\beta = \begin{cases} 0 & (n \text{ even}), \\ 1 & (n \text{ odd}). \end{cases} \tag{36}$$

These vector fields include the Chebyshev factor $(1-r^2)^{-1/2}$ and suitable monomials so that the symmetrization rule (31) holds. Therefore, the products between the test and trial functions can be exactly calculated via *Gauss–Lobatto* quadrature, leading to banded matrices. Since the test and trial functions are not the same, this projection procedure is usually known as *Petrov–Galerkin* scheme.

In the radial coordinate, we consider the Gauss–Lobatto points

$$r_k = -\cos\left(\frac{\pi k}{M_r}\right), \quad k = 0, \ldots, M_r, \tag{37}$$

where we will assume that $M_r$ is *odd* and of suitable order so that the quadratures are exact. The spectral differentiation matrix is given by

$$(\mathbb{D}_r)_{ij} = \begin{cases} (1+2M_r^2)/6 & i = j = M_r, \\ -(1+2M_r^2)/6 & i = j = 0, \\ -\frac{r_i}{2(1-r_i^2)} & i = j;\ 0 < i < M_r, \\ (-1)^{i+j}\frac{c_j}{c_i(r_j-r_i)} & i \neq j, \end{cases} \tag{38}$$

where $c_j = 1$ for $0 < j < M_r$ and $c_0 = c_{M_r} = 2$ [3,25]. The radial, azimuthal and axial components of the trial functions $\boldsymbol{\Phi}^{(1,2)}_{lnm}$ are either *even* or *odd* functions of $r$. Therefore, we only need to consider the positive part of the grid

$$r_k^+ = -\cos\left(\frac{\pi k}{M_r}\right), \quad k = \frac{M_r+1}{2}, \dots, M_r. \tag{39}$$

For arbitrary even, $\mathrm{f_e}(r)$, or odd, $\mathrm{f_o}(r)$, functions satisfying

$$\mathrm{f_e}(r_k) = \mathrm{f_e}(r_{M_r-k}), \quad \mathrm{f_o}(r_k) = -\mathrm{f_o}(r_{M_r-k}), \quad k = 0, \dots, \frac{M_r-1}{2}, \tag{40}$$

the differentiation matrices which provide the first derivatives

$$\left(\frac{\mathrm{df_e}}{\mathrm{d}r}\right)_{r=r_i^+} = \left(\mathbb{D}_r^{\mathrm{e}}\right)_{ij}\mathrm{f_e}(r_j^+), \qquad \left(\frac{\mathrm{df_o}}{\mathrm{d}r}\right)_{r=r_i^+} = \left(\mathbb{D}_r^{0}\right)_{ij}\mathrm{f_o}(r_j^+), \tag{41}$$

are obtained from the Chebyshev matrix (38):

$$\left(\mathbb{D}_r^{\mathrm{e}}\right)_{ij} = (\mathbb{D}_r)_{ij} + (\mathbb{D}_r)_{iM_r-j}, \quad i, j = \frac{M_r+1}{2}, \dots, M_r, \tag{42}$$

and

$$\left(\mathbb{D}_r^{0}\right)_{ij} = (\mathbb{D}_r)_{ij} - (\mathbb{D}_r)_{iM_r-j}, \quad i, j = \frac{M_r+1}{2}, \dots, M_r. \tag{43}$$

For the periodic azimuthal and axial coordinates, we use standard equispaced grids

$$(z_i, \theta_j) = \left(\frac{Q}{L_z} i, \frac{2\pi}{N_\theta} j\right), \quad (i, j) = [0, L_z - 1] \times [0, N_\theta - 1], \tag{44}$$

where we assume that $N_\theta$ and $L_z$ are odd, and we make use of the standard Fourier matrix [8] for the differentiation of fields with respect to those variables.

## 4. Dynamical system of amplitudes

The spectral Petrov–Galerkin scheme is accomplished by substituting expansion (17) in (11) and projecting over the set of test vector fields (32)–(33) and (34)–(35)

$$(\boldsymbol{\Psi}_{lnm}, \partial_t \mathbf{u}_\mathrm{S}) = \left(\boldsymbol{\Psi}_{lnm}, \frac{1}{Re}\Delta\mathbf{u}_\mathrm{S} - (\mathbf{v}_\mathrm{B}\cdot\nabla)\mathbf{u}_\mathrm{S} - (\mathbf{u}_\mathrm{S}\cdot\nabla)\mathbf{v}_\mathrm{B} - (\mathbf{u}_\mathrm{S}\cdot\nabla)\mathbf{u}_\mathrm{S}\right), \tag{45}$$

for $l = -L, \dots, L$, $n = -N, \dots, N$ and $m = 0, \dots, M$. We have not included the pressure term $\nabla q$ of (11) in the projection scheme (45). One of the advantages of our method is that the pressure term is cancelled in the projection, i.e.,

$$(\boldsymbol{\Psi}_{lnm}, \nabla q) = 0; \tag{46}$$

see [4] or [14], for example.

Once the projection has been carried out, the spatial dependence has been eliminated from the problem and a nonlinear dynamical system for the amplitudes $a_{lnm}$ is obtained. Symbolically, this system reads

$$\mathbb{A}^{lnm}_{pqr}\dot{a}_{pqr} = \mathbb{B}^{lnm}_{pqr}a_{pqr} - b_{lnm}(a, a), \tag{47}$$

where we have used the convention of summation with respect to repeated subscripts. The discretized operator $\mathbb{A}$ appearing in (47) is the projection

$$\mathbb{A}^{lnm}_{pqr} = (\boldsymbol{\Psi}_{lnm}, \boldsymbol{\Phi}_{pqr}) = 2\pi Q\delta^l_p\delta^n_q\int_0^1 \tilde{\mathbf{v}}^*_{lnm}\cdot\mathbf{v}_{pqr} r\,\mathrm{d}r, \tag{48}$$

where $\delta^i_j$ is the Kronecker symbol. The inner product (48) reveals another advantage of the Galerkin scheme. Due to the linearity of the time differentiation operator $\partial_t$ and the Fourier orthogonality in the periodic variables, the axial and azimuthal modes decouple. The operator $\mathbb{B}$ in (47),

$$\mathbb{B}^{lnm}_{pqr} = \left(\boldsymbol{\Psi}_{lnm}, \frac{1}{Re}\Delta\boldsymbol{\Phi}_{pqr} - (\mathbf{v}_{\mathrm{B}}\cdot\nabla)\boldsymbol{\Phi}_{pqr} - (\boldsymbol{\Phi}_{pqr}\cdot\nabla)\mathbf{v}_{\mathrm{B}}\right), \tag{49}$$

satisfies the same orthogonality properties in the periodic variables. As a result, those operators $\mathbb{A}^{lnm}_{pqr}$ and $\mathbb{B}^{lnm}_{pqr}$ with different axial indices ($l \neq p$) or different azimuthal ones ($n \neq q$) are identically zero. The remaining operators with $l = p$ and $n = q$ have a banded structure due to the orthogonality properties of the shifted Chebyshev basis used in the radial variable. In Fig. 2 we have represented the sparse structure of both operators for the particular case $l = p = 1$ and $n = q = 1$. A clever reordering of the vector of coefficients makes $\mathbb{A}$ and $\mathbb{B}$ collapse into a single band structure. The quadratic form $b_{lnm}(a, a)$ appearing in (47) corresponds to the projection of the nonlinear convective term

$$\big(\boldsymbol{\Psi}_{lnm}, (\mathbf{u}_{\mathrm{S}}\cdot\nabla)\mathbf{u}_{\mathrm{S}}\big). \tag{50}$$

For computational efficiency, this term has to be calculated via a pseudospectral method. The details of this computation will be analyzed later. Finally, the initial value problem is prescribed by the coefficients $a_{lnm}(0)$ representing the initial vector field $\mathbf{u}^0_{\mathrm{S}}$ given by

$$a_{lnm}(t = 0) = \big(\boldsymbol{\Psi}_{lnm}, \mathbf{u}^0_{\mathrm{S}}\big). \tag{51}$$

## 5. Linear stability

The stability of very small perturbations added to the basic flow is dictated by the linearized equation

$$\mathbb{A}^{lnm}_{pqr}\dot{a}_{pqr} = \mathbb{B}^{lnm}_{pqr}a_{pqr}, \tag{52}$$

obtained from (47), where we have neglected the nonlinear advective term. Therefore, since the problem is linear, we can decouple the eigenvalue analysis for each independent azimuthal-$n$ and axial-$l$ wavenumbers associated with the $\mathrm{e}^{\mathrm{i}(n\theta+kz)}$ *normal mode*, where $k = l\mathrm{k}_0$. For a fixed axial and azimuthal periodicity, the spectrum is given by the eigenvalues of the operator $\mathbb{L} = \mathbb{A}^{-1}\mathbb{B}$,

$$\mathbb{L}\mathbf{a} = \lambda\mathbf{a}, \tag{53}$$

where the operators $\mathbb{A}$ and $\mathbb{B}$ are the matrices (48) and (49) corresponding to the axial-azimuthal mode $(n, l)$ under study, $\lambda$ is an eigenvalue of the spectrum of $\mathbb{L}$, and $\mathbf{a}$ is its associated *eigenvector*

$$\mathbf{a} = \big(a^{(1)}_1, \ldots, a^{(1)}_M, a^{(2)}_1, \ldots, a^{(2)}_M\big)^{\mathrm{T}}, \tag{54}$$

where we have omitted the axial and azimuthal subscripts for simplicity.

The convergence and reliability of the spectral method have been checked. For this purpose, some of the results reported here have been compared with previous works. For example, in Table 1, the convergence of the least stable eigenvalue has been tested for $Re = 9600$, $n = 1$ and $k = 1$, a case previously studied by other authors [14,20]. For $Re = 3000$, the spectra for different values of $k$ and $n$ have been computed in order to make comparisons with a first comprehensive linear stability analysis carried out in [22]. Our code provided spectral accuracy in all the computed cases. In Tables 2 and 3, the spectra of the 10 rightmost eigenvalues have been listed for $(k = 1, n = 0, 1)$ and $(k = 1, n = 2, 3)$, respectively, following Schmid and Henningson's former study.

The same computation has been done for *streamwise-independent* perturbations ($k = 0$) and for different values of the azimuthal mode $n$ (see Table 4). To the author's knowledge, numerical tables of streamwise-independent modes have not been reported previously. Mathematically, the case $k = 0$ needs a special treatment. In fact, the limit $k \to 0$ does not coincide with this case. In our formulation, this phenomenon can be understood looking at the boundary conditions which must be satisfied by the radial velocity over the wall. For $k \neq 0$, the radial velocity, as well as its first derivative, must vanish over the wall. For $k = 0$ the boundary conditions change abruptly.

Our formulation in solenoidal primitive vector fields allows to obtain the explicit expression of a *first integral* of the perturbation field, i.e., a manifold over which the fluid particles lie on for all $t$. The obtention of a closed form of these

Table 1
Convergence test for $Re = 9600$, $k = 1$ and $n = 1$, following [14] and [20]

| $M$ | *size* | $\lambda_1$ | | |
|---|---|---|---|---|
| 20 | $42 \times 42$ | −0.0229 | + | i0.950 |
| 30 | $62 \times 62$ | −0.0231707 | + | i0.9504813 |
| 40 | $82 \times 82$ | −0.02317079576 | + | i0.950481396669 |
| 50 | $102 \times 102$ | −0.023170795764 | + | i0.950481396670 |

| | |
|---|---|
| Leonard & Wray (1982) | $\lambda_1 = -0.023170795764 + \mathrm{i}0.950481396668$ |
| Priymak & Miyazaki (1998) | $\lambda_1 = -0.023170795765 + \mathrm{i}0.950481396670$ |

$M$ is the number of Chebyshev polynomials used in our spectral approximation, *size* is the dimension of the discretization matrices appearing in Fig. 2 and $\lambda_1$ stands for the rightmost eigenvalue. The reported figures are those which apparently converged at $M = 60$.

Table 2
Rightmost eigenvalues for $Re = 3000$, $k = 1$ and $n = 0, 1$, following [22]

| $n = 0$ | | | $n = 1$ | | |
|---|---|---|---|---|---|
| −0.0519731112828 | + | i0.9483602220505 | −0.041275644693 | + | i0.91146556762 |
| −0.0519731232053 | + | i0.948360198487 | −0.0616190180049 | + | i0.370935092697 |
| −0.103612364039 | + | i0.896719200867 | −0.088346025188 | + | i0.958205542989 |
| −0.103612889227 | + | i0.8967204441 | −0.0888701566 | + | i0.8547888174 |
| −0.112217160388 | + | i0.4123963342099 | −0.1168771535871 | + | i0.216803862997 |
| −0.121310028246 | + | i0.2184358147279 | −0.137490337 | + | i0.7996994696 |
| −0.155220165293 | + | i0.8450717997117 | −0.14434614486 | + | i0.91003730954 |
| −0.155252667198 | + | i0.845080668126 | −0.1864329862 | + | i0.7453043578 |
| −0.2004630477669 | + | i0.3762423600255 | −0.195839466 | + | i0.5493115826 |
| −0.20647681141 | + | i0.79378412983 | −0.198646109 | + | i0.8607494634 |

The reported figures are apparently converged at $M = 54$.

Table 3
Same as Table 2 for $n = 2, 3$

| $n = 2$ | | | $n = 3$ | | |
|---|---|---|---|---|---|
| −0.060285689559 | + | i0.88829765875 | −0.08325397694 | + | i0.86436392104 |
| −0.08789898037 | + | i0.352554927087 | −0.105708407362 | + | i0.346401953386 |
| −0.1088383407 | + | i0.8328933609 | −0.116877921343 | + | i0.2149198697617 |
| −0.112001616152 | + | i0.939497219531 | −0.1323924331 | + | i0.8097468023 |
| −0.1155143802215 | + | i0.215491816529 | −0.136035459528 | + | i0.91671917468 |
| −0.15810861 | + | i0.778584987 | −0.182036372 | + | i0.7558793156 |
| −0.167294045951 | + | i0.8906185726 | −0.190639836903 | + | i0.8674136555 |
| −0.20759146658 | + | i0.725077139 | −0.2127794121 | + | i0.37123649827 |
| −0.20931432998 | + | i0.37502653759 | −0.23181786 | + | i0.70300722 |
| −0.2214747313 | + | i0.8409753749 | −0.244111241 | + | i0.551731632 |

stream functions is possible because of the $(\theta, z)$ invariance transformation induced by the normal mode analysis. The normal mode $\mathrm{e}^{\mathrm{i}(n\theta + kz)}$ is invariant under *spiral* transformations of the form:

$$\frac{\mathrm{d}z}{\mathrm{d}\theta} = -\frac{n}{k}. \tag{55}$$

We define a *spiral variable* $\zeta \doteq n\theta + kz$, so that the solenoidal condition

$$\nabla \cdot \mathbf{v} = \frac{1}{r}\partial_r(r v_r) + \frac{1}{r}\partial_\theta v_\theta + \partial_z v_z = 0$$

can be expressed as

$$\partial_r(r v_r) + \partial_\zeta[n v_\theta + r k v_z] = 0, \tag{56}$$

Table 4
Same as Tables 2, 3 for $k = 0$, $n = 0, 1, 2, 3$

| $n = 0$ | $n = 1$ | $n = 2$ | $n = 3$ |
|---|---|---|---|
| −0.0019277286542 | −0.00489399021 | −0.0087915387 | −0.0135688219 |
| −0.004893990214 | −0.0087915388 | −0.01356882195 | −0.01919431362 |
| −0.0101570874478 | −0.0164061521 | −0.0236166663 | −0.03175919084 |
| −0.01640615210723 | −0.0236166663 | −0.03175919085 | −0.040809265355 |
| −0.0249623355969 | −0.03449981796 | −0.04500690295 | −0.0564651499 |
| −0.034499817965 | −0.045006902955 | −0.05646514994 | −0.06885660345 |
| −0.0463467614754 | −0.059173588937 | −0.0729733963 | −0.087733618 |
| −0.0591735889378 | −0.072973396381 | −0.08773361808 | −0.103440753288 |
| −0.07431076787255 | −0.090427218091 | −0.1075183721 | −0.1255751331 |
| −0.0904272180909 | −0.107518372097 | −0.12557513314 | −0.14458704546 |

where we have used the differentiation rules

$$\partial_\theta = (\partial_\theta \zeta)\partial_\zeta = n\partial_\zeta, \qquad \partial_z = (\partial_z \zeta)\partial_\zeta = k\partial_\zeta.$$

Eq. (56) defines implicitly a first integral $\Theta(r, \zeta)$ satisfying

$$\partial_\zeta \Theta = -r v_r, \tag{57}$$

and

$$\partial_r \Theta = n v_\theta + r k v_z. \tag{58}$$

A straightforward integration of (58) leads to the explicit expression of $\Theta$ for cases I and II described in Section 3. The physical vector field is a real object obtained from solving the eigenvalue problem (53) associated with the normal mode $e^{i(n\theta+kz)}$ and its conjugated:

$$\mathbf{u} = 2\Re\left\{ e^{i(kz+n\theta)} \sum_{m=0}^{M} a_m^{(1)} \mathbf{v}_m^{(1)} + a_m^{(2)} \mathbf{v}_m^{(2)} \right\}, \tag{59}$$

where the subscripts $l$ and $n$ have been omitted for simplicity. From Eqs. (24)–(27) and (58) we can obtain explicit expressions for the first integral $\Theta$:

I. *Axisymmetric fields* ($n = 0$):

$$\Theta(r, \theta, z) = 2kr^2 \Re\left\{ e^{ikz} \sum_{m=0}^{M} a_m^{(2)} g_m(r) \right\}, \tag{60}$$

except that $\Theta$ is a constant if $k = 0$.

II. *Non-axisymmetric fields* ($n \neq 0$):

$$\Theta(r, \theta, z) = 2nr^\sigma \Re\left\{ e^{i(kz+n\theta)} \sum_{m=0}^{M} a_m^{(1)} g_m(r) \right\}, \tag{61}$$

for all $k$.

In Fig. 3 we have represented the spectrum of eigenvalues computed for $Re = 3000$, $n = 1$ and $k = 1$. Three different branches are clearly identified; wall modes branch (WM), center modes branch (CM) and mean modes branch (MM) [7,6]. In order to have a qualitative idea of the dynamics associated with each one of the three branches, we have plotted the velocity field $\mathbf{v}$ computed from (59) and the first integral obtained from (61) in Fig. 4, for the three selected eigenvalues in Fig. 3. In particular, we have represented the eigenfunctions corresponding to the *wall*, *center* and *mean* eigenvalues previously shown in Fig. 3. The pictures corresponding to the center and wall modes shown in Fig. 4 have recently appeared in [6].

## 6. Nonlinear unsteady computations

### 6.1. Overview

The spectral spatial discretization of the Navier–Stokes equations leads to a *stiff* system of ODEs [3,9,10], characterized by the presence of modes with vastly different time-scales. This pathology leads to stability problems in the time discretization, in particular when explicit time integration schemes are used. The development of numerical algorithms for the solution of stiff systems is an active research area where new methodologies appear frequently. In spectral discretization of nonlinear PDEs, the more standard procedures are based on *semi-implicit*, also called *linearly implicit* methods, where the linear part is integrated implicitly and the nonlinear terms are treated explicitly. In a recent work [5], *Exponential Time Differencing* (ETD) schemes were proved to be more efficient for some stiff PDES, in comparison with standard linearly implicit, integrating factor or splitting methods. Nevertheless, ETD methods lead to technical complications when the domain of the problem has no periodicity or when the linearized operator $\mathbb{L}$ appearing in Eq. (53) is (or is close to be) singular. For moderately high Reynolds numbers, the ill-conditioning of the linearized Navier–Stokes operator and the radial-Chebyshev spectral interpolation make the ETD scheme not feasible for practical purposes.

Second- and fourth-order linearly implicit time integration schemes have been tested for unsteady computations of transitional regimes in pipe flow. In particular, implicit *Backward Differences*, combined with modified *Adams–Bashforth* polynomial extrapolation (also termed AB2BD2 and AB4BD4 in [5]), have been used. It is well known that BD4 method may lead to stability problems [9]. Nevertheless, we found AB4BD4 as the best scheme for this particular problem.

### 6.2. Linearly implicit time integration

Let $\Delta t$ be the time step and $t^{(k)} = k\Delta t$, $k = 0, 1, 2, \ldots,$ the time array where we approximate our amplitudes $a(t)$[1] from the original system (47). In our notation, $a^{(k)} = a(t^{(k)})$ is the approximation of $a(t)$ at $t = t^{(k)}$ and $b^{(k)}$ is the nonlinear quadratic form appearing in (47) evaluated at $t^{(k)}$, i.e., $b^{(k)} = b(a^{(k)}, a^{(k)})$. The second order AB2BD2 method is given by the iteration

$$(3\mathbb{A} - 2\Delta t\mathbb{B})a^{(k+1)} = \mathbb{A}\bigl(4a^{(k)} - a^{(k-1)}\bigr) - 2\Delta t\bigl(2b^{(k)} - b^{(k-1)}\bigr), \tag{62}$$

for $k \geqslant 1$, see [5], whereas the fourth-order AB4BD4 scheme is

$$\begin{aligned}(25\mathbb{A} - 12\Delta t\mathbb{B})a^{(k+1)} &= \mathbb{A}\bigl(48a^{(k)} - 36a^{(k-1)} + 16a^{(k-2)} - 3a^{(k-3)}\bigr)\\ &\quad - \Delta t\bigl(48b^{(k)} - 72b^{(k-1)} + 48b^{(k-2)} - 12b^{(k-3)}\bigr),\end{aligned} \tag{63}$$

for $k \geqslant 3$. In both schemes, the initial value $a^{(0)}$ is prescribed by the initial condition (51), and the first unknown amplitudes, $a^{(1)}$ for (62) or $a^{(1,2,3)}$ for (63), are obtained by means of a fourth-order *Runge–Kutta* explicit method.

The nonlinear explicit contributions $b^{(k)}$ appearing in (62) and (63) must be efficiently computed in advance by means of a *de-aliased* pseudospectral or collocation method. The main goal is to compute the term

$$b_{lnm} = \bigl(\boldsymbol{\Psi}_{lnm}, (\mathbf{u}_S \cdot \nabla)\mathbf{u}_S\bigr) = \int_0^Q \int_0^{2\pi} \int_0^1 \boldsymbol{\Psi}^*_{lnm} \cdot (\mathbf{u}_S \cdot \nabla)\mathbf{u}_S r \,\mathrm{d}r \,\mathrm{d}\theta \,\mathrm{d}z, \tag{64}$$

where $\mathbf{u}_S$ is given by the known coefficients $a^{(k)}$ appearing in expansion (17), at a previous stage in time. The standard procedure for the computation of the nonlinear advective term is summarized in the diagram of Fig. 1.

Basically, once the coefficients $a_{lnm}$ (top left of the diagram) of $\mathbf{u}_S$ are known, we evaluate $\mathbf{u}_S$ in the physical space (top arrow going from left to right in the diagram). The gradient of the vector field, $\nabla\mathbf{u}_S$, and the convective product, $(\mathbf{u}_S \cdot \nabla)\mathbf{u}_S$ , are also computed in the physical space (vertical arrows downwards, on the right). Finally, the physical

---

[1] To avoid cumbersome notation, we temporarily suppress the subscripts corresponding to the spatial discretization.

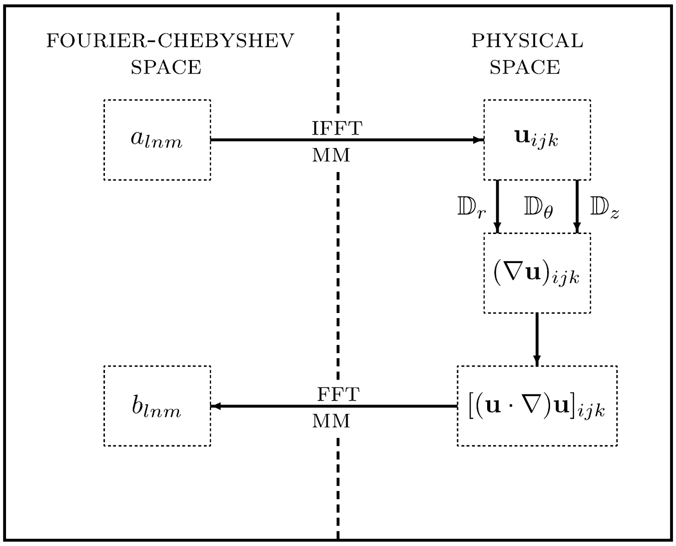

Fig. 1. Pseudospectral computation of nonlinear terms. The abbreviations FFT, IFFT and MM stand for *Fast Fourier Transform*, *Inverse Fast Fourier Transform* and *Matrix Multiplication*, respectively.

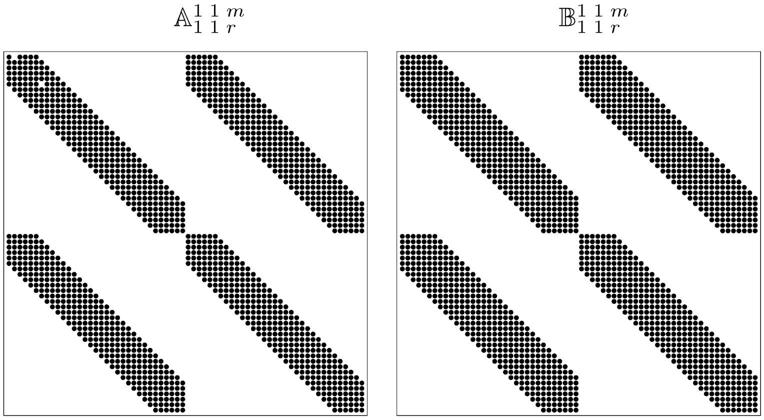

Fig. 2. Sparse structure of operators $\mathbb{A}^{lnm}_{pqr}$ and $\mathbb{B}^{lnm}_{pqr}$ for $l = p = 1$ and $n = q = 1$, with $M = 32$ radial modes.

product is projected onto the dual Fourier–Chebyshev space (bottom arrow, from right to left). The first stage of the algorithm is to evaluate the sum (17)

$$\mathbf{u}_S = \sum_{l=-L}^{L}\sum_{n=-N}^{N}\sum_{m=0}^{M} a_{lnm}(t)\boldsymbol{\Phi}_{lnm}(r,\theta,z) = \sum_{l=-L}^{L}\sum_{n=-N}^{N}\sum_{m=0}^{M} a_{lnm}\mathrm{e}^{\mathrm{i}(n\theta+\mathrm{k}_0 lz)}\mathbf{v}_{lnm}(r) \tag{65}$$

over the three-dimensional grid

$$(r_k,\theta_j,z_i) = \left(\cos\left(\frac{\pi k}{2M_d}\right), \frac{2\pi}{N_d}j, \frac{Q}{L_d}i\right), \tag{66}$$

for $k = 0,\ldots,M_d - 1$, $j = 0,\ldots,N_d - 1$ and $i = 0,\ldots,L_d - 1$. The values $M_d$, $N_d$ and $L_d$ are the numbers of radial, azimuthal and axial points, respectively, needed to *de-alias* the computation up to the spectral order of $\mathbf{u}_S$. For coarse grid computations, the convolution sums which appear when evaluating the nonlinear terms may generate low *aliased*

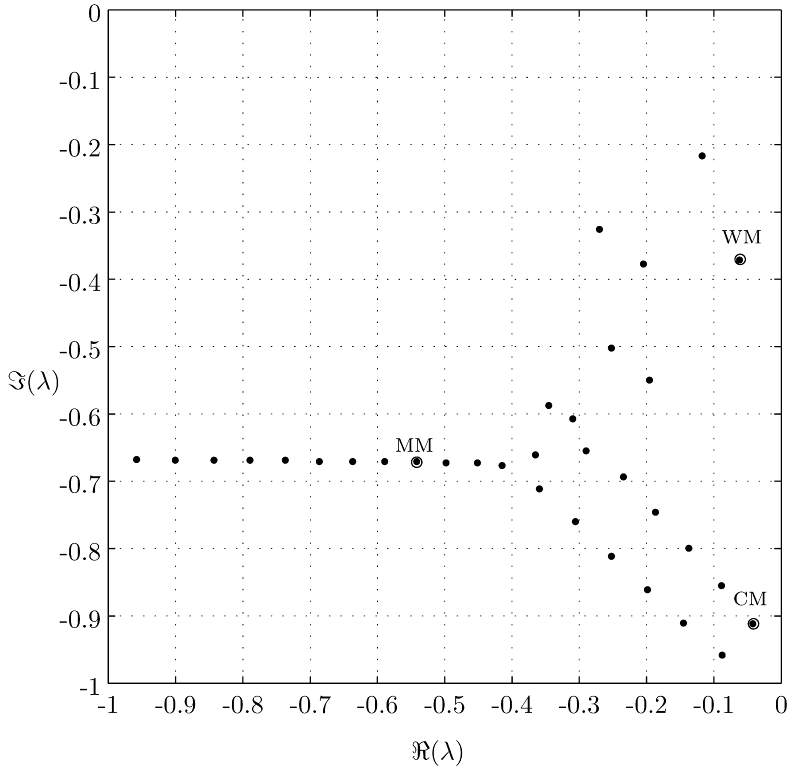

Fig. 3. Spectrum of eigenvalues for $Re = 3000$, $n = 1$, $k = 1$. The labelled dots WM (wall mode), CM (center mode) and MM (mean mode) are the eigenvalues whose associated eigenfunctions have been plotted in Fig. 4.

modes [4]. A similar problem arises in the non-periodic (radial) direction, although in this case it is related to a poorly resolved quadrature. In this method, aliasing is removed by means of Orszag's $\frac{3}{2}$-rule, imposing

$$L_d \geqslant \frac{3}{2}(2L+1), \qquad N_d \geqslant \frac{3}{2}(2N+1), \qquad M_d \geqslant 3M, \tag{67}$$

in order to eliminate aliased modes up to order $(L, N, M)$. Direct evaluation of (65) over each point of the grid (66) would require $O(LMN)$ operations. Overall, the total computation of $\mathbf{u}_S$ would imply a total number of operations of order $O(L^2N^2M^2)$. Nevertheless, we can substantially reduce the number of operations by means of *Partial Summation* technique [3], where $\mathbf{u}_S$ ($\mathbf{u}$ for simplicity) is evaluated over the radial grid $r_k$:

$$\mathbf{u}_k(\theta, z) = \mathbf{u}(r_k, \theta, z) = \sum_{l=-L}^{L} \sum_{n=-N}^{N} e^{i(n\theta + k_0 l z)} \underbrace{\sum_{m=0}^{M} a_{lnm} \mathbf{v}_{lnm}(r_k)}_{\alpha_{ln}^{(k)}}, \quad k \in [0, M_d - 1]. \tag{68}$$

The sum for the radial modes in (68) has been underbraced and identified by the coefficients $\alpha_{ln}^{(k)}$, that require $O(M^2LN)$ operations to be computed. The second step is the evaluation of $\mathbf{u}_k(\theta, z)$ over the azimuthal grid

$$\mathbf{u}_{jk}(z) = \mathbf{u}(r_k, \theta_j, z) = \sum_{l=-L}^{L} e^{il k_0 z} \underbrace{\sum_{n=-N}^{N} \sum_{m=0}^{M} a_{lnm} e^{in\theta_j} \mathbf{v}_{lnm}(r_k)}_{\beta_l^{(jk)}}, \quad (j, k) \in [0, N_d - 1] \times [0, M_d - 1], \tag{69}$$

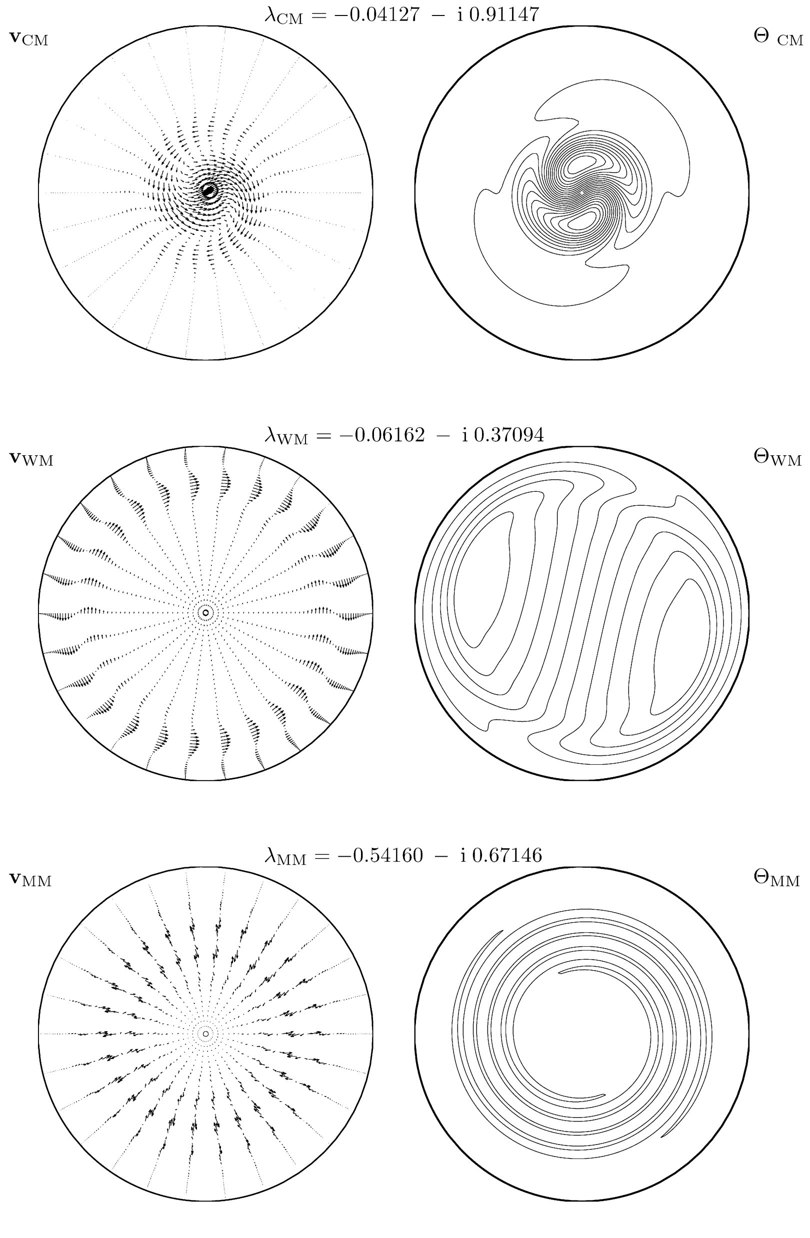

Fig. 4. Eigenmodes corresponding to the three selected eigenvalues of Fig. 3.

taking advantage of the pre-computed $\alpha_{ln}^{(k)}$ coefficients,

$$\beta_l^{(jk)} = \sum_{n=-N}^{N} \mathrm{e}^{\mathrm{i}n\theta_j} \sum_{m=0}^{M} a_{lnm} \mathbf{v}_{lnm}(r_k) = \sum_{n=-N}^{N} \mathrm{e}^{\mathrm{i}n\theta_j} \alpha_{ln}^{(k)}, \tag{70}$$

that requires $\mathrm{O}(N^2ML)$ operations. Finally, $\mathbf{u}_{jk}(z)$ over the axial grid $z_i$ is computed using the same procedure, i.e.,

$$\mathbf{u}_{ijk} = \mathbf{u}(r_k, \theta_j, z_i) = \sum_{l=-L}^{L} \mathrm{e}^{\mathrm{i}k_0 l z_i} \beta_l^{(jk)}, \quad (i, j, k) \in [0, L_d - 1] \times [0, N_d - 1] \times [0, M_d - 1]. \tag{71}$$

Overall, the computational cost needed for the previous three stages is $\mathrm{O}(LNM(L+N+M))$, and it can be further improved by using the FFT in $z$ and FCT (*Fast Cosine Transform*) in $r$, leading to an optimal cost of $\mathrm{O}(LNM\ln(LNM))$

operations per time step. Computation of $(\mathbf{u}_{\mathrm{S}} \cdot \nabla)\mathbf{u}_{\mathrm{S}}$ in the physical space is carried out by using standard Fourier Differentiation matrices [8] in the axial and azimuthal coordinates, whereas differentiation matrices $\mathbb{D}_r^{\mathrm{e,o}}$ defined in (43)–(42) are used in the radial direction. Finally, partial summation techniques are used again to efficiently inverse-transform of $[(\mathbf{u}_{\mathrm{S}} \cdot \nabla)\mathbf{u}_{\mathrm{S}}]_{ijk}$ leading to the nonlinear term $b_{lnm}$ appearing in (47).

## 7. Validation of the numerical scheme

### 7.1. Convergence analysis

The spatial convergence of the spectral Petrov–Galerkin method has already been tested in Section 5 and also in [17] via a linear asymptotic eigenvalue analysis, providing spectral accuracy in all cases studied. For the nonlinear unsteady computations, the same initial value problem has been solved by means of the two different linearly implicit schemes AB2BD2 and AB4BD4. In both cases, the same spectral resolution in space, the same initial condition for the amplitudes and the same total integration time have been considered for consistency. In particular, the initial perturbation that we considered for our convergence tests is a two-dimensional streamwise independent field of the form

$$\mathbf{u}_{\mathrm{S}}^0 = \mathbf{u}_{\mathrm{2D}}^0 = \mathrm{A}_{\mathrm{2D}} \mathrm{e}^{\mathrm{i}\theta}\big(-\mathrm{i} f_1(r), f_2(r), 0\big) + \mathrm{c.c.}, \tag{72}$$

where $f_1(r) = 1 - 2r^2 + r^4$, $f_2(r) = 1 - 6r^2 + 5r^4$, c.c. stands for complex conjugate and $\mathrm{A}_{\mathrm{2D}}$ is a real constant such that $\boldsymbol{\varepsilon}(\mathbf{u}_{\mathrm{S}}^0) = \boldsymbol{\varepsilon}_0$, where $\boldsymbol{\varepsilon}(\mathbf{u})$ is the *normalized energy* of an arbitrary perturbation,

$$\boldsymbol{\varepsilon}(\mathbf{u}) = \frac{1}{2\mathrm{E}_{\mathrm{HP}}} \int_0^{Q} \mathrm{d}z \int_0^{2\pi} \mathrm{d}\theta \int_0^1 r\,\mathrm{d}r\,\mathbf{u}^* \cdot \mathbf{u}, \tag{73}$$

with respect to the energy of the basic Hagen–Poiseuille flow, $\mathrm{E}_{\mathrm{HP}} = \pi Q/6$. The initial condition (72) consists of a pair of streamwise vortices of azimuthal number $n = 1$ that only perturb the radial and the azimuthal components of the basic regime. This perturbation has streamwise invariance in time, due to its orthogonality with respect to the axial base flow. Thus, the initial condition ensures that $\mathbf{u}_{\mathrm{S}}(t)$ preserves its streamwise symmetry for all $t$. In Fig. 5(a) we have plotted a $z$-cnst. cross section of the perturbation field $\mathbf{u}_{\mathrm{S}}^0$, and the basic parabolic profile of the Hagen–Poiseuille flow has been represented in Fig. 5(b). Finite amplitude perturbations of the form (72) are of special interest in the nonlinear stability analysis of shear flows. Streamwise vortices are particularly efficient in triggering transition due to the usually termed *lift-up* effect, advecting slow axial flow to high speed regions and vice versa [12,21,23,26]. This mechanism modulates the axial parabolic flow in a new transient profile, usually termed *streak*, which contains saddle points, thus being potentially unstable with respect to three-dimensional infinitesimal disturbances [6,7,23].

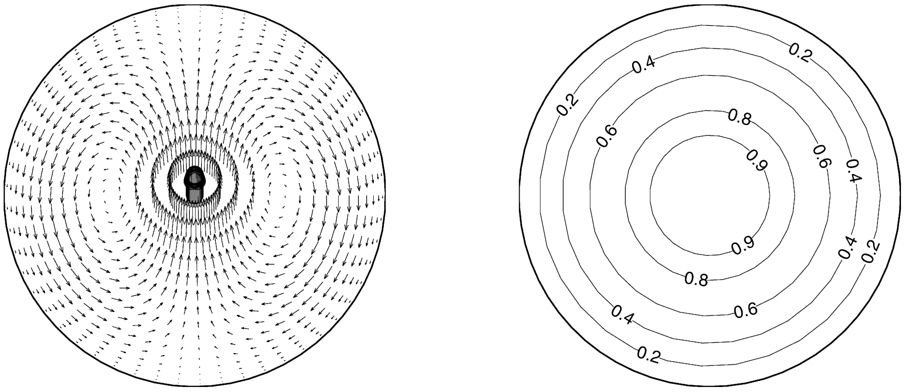

(a) (b)

Fig. 5. (a) Initial perturbation field $\mathbf{u}_{\mathrm{S}}^0$ prescribed by amplitudes given in (72). (b) Contour level curves of the axial speed corresponding to the parabolic Hagen–Poiseuille flow.

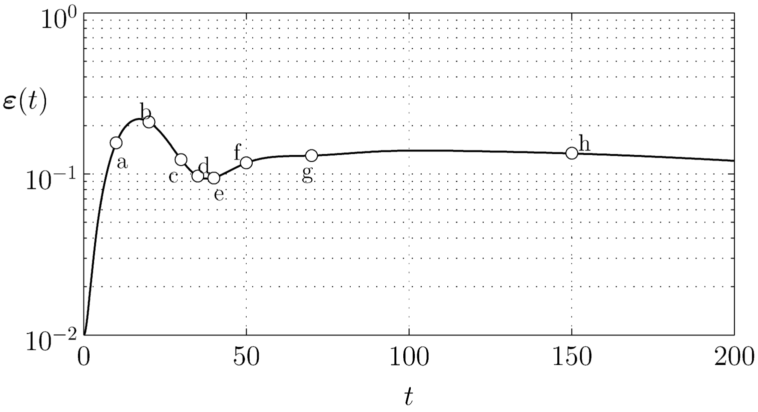

Fig. 6. Typical evolution of the energy of a two-dimensional streamwise perturbation.

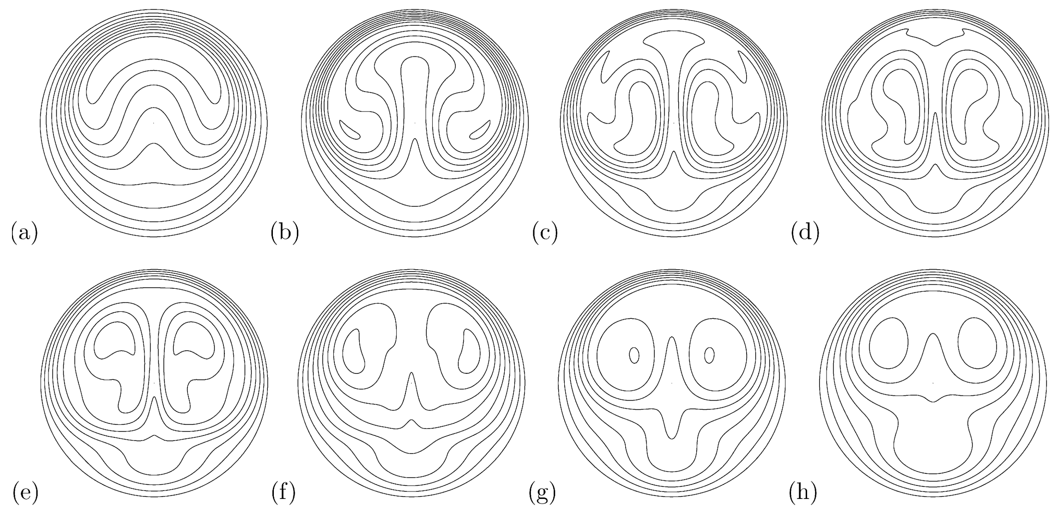

Fig. 7. Modulated axial speed $(\mathbf{u}_{\mathrm{S}} + \mathbf{v}_{\mathrm{B}})_z$ contours corresponding to the time integration plotted in Fig. 6.

As an example, Fig. 6 shows the evolution of the energy $\boldsymbol{\varepsilon}(t)$ associated with the two-dimensional perturbation prescribed in Eq. (72) for $Re = 3000$ and with initial energy $\boldsymbol{\varepsilon}(\mathbf{u}_{\mathrm{S}}^0) = \boldsymbol{\varepsilon}_0 = \boldsymbol{\varepsilon}(0) = 10^{-2}$. The structure of the modulated axial flow has been represented in Fig. 7 at some selected instants of time, labeled with white circles in Fig. 6. This run was carried out using AB4BD4 with $M \times N = 25 \times 15$ radial × azimuthal modes (equivalent to $M_r \times N_\theta = 26 \times 31$ collocation points), with $\Delta t = 0.01$ and a total integration time $T = 200$. The evolution of this kind of perturbations was originally considered in [26], where hybrid 2nd order finite differences scheme in $r$ combined with a spectral Fourier method in $\theta$ was used. Low spatial resolution simulations based on the present spectral method were also provided in [16]. In both cases the agreement with former computations is very good. In Fig. 7 it is clearly observed the formation of streaks. The first important feature of this transient flow is the presence of saddle points in its profile. The second is that this transient regime is almost steady, as we observe more clearly from the curve in Fig. 6.

A time-convergence test has been carried out by comparing the accuracy of the solution for the AB2BD2 and AB4BD4 schemes, always based on the same kind of perturbations described before. All the runs have been based on the same initial condition (72), for $Re = 2500$, $M = 10$, $N = 10$ and a total time $T = 50$. Fig. 8 captures the essential features of the convergence of the two different time marching schemes, representing the absolute $L_2$-norm error of

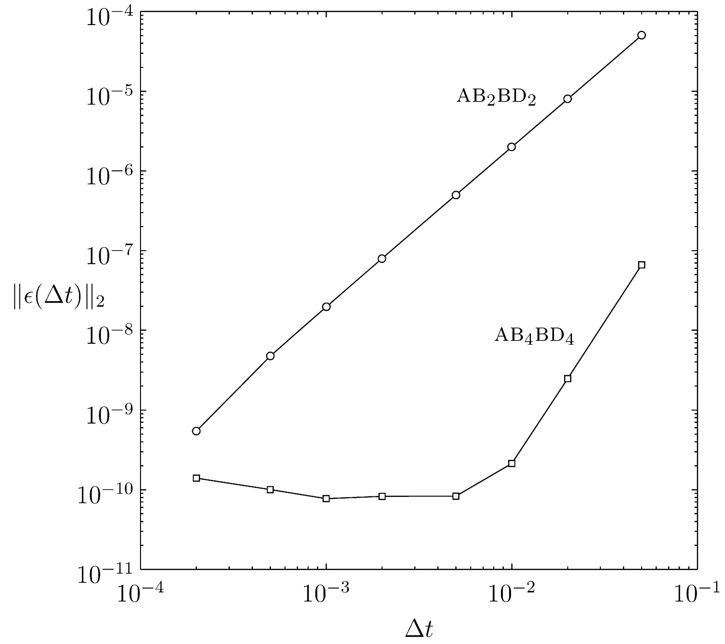

Fig. 8. Absolute error (74) for the two different time marching schemes. The two curves represent the error obtained for the same initial value problem and with the same spatial resolution.

the Fourier coefficients $a_{lnm}^{\Delta t}(T)$ obtained at the end of the run with respect to the "*exact*" ones, $a_{lnm}^{\Delta t_0}(T)$, obtained with a much smaller reference time step $\Delta t_0 = 10^{-4}$,

$$\left\|\epsilon(\Delta t)\right\|_2^2 = \sum_{l,n,m} \left|a_{lnm}^{\Delta t}(T) - a_{lnm}^{\Delta t_0}(T)\right|^2. \tag{74}$$

Fig. 8 reveals a faster (and better) convergence of the fourth order scheme in front of the second order one. In fact, for $\Delta t < 10^{-2}$, the AB2BD2 scheme is still converging with an absolute error of order $10^{-6}$, whereas the AB4BD4 has already achieved the accuracy dictated by the spatial resolution. When using AB2BD2, $\Delta t$ should still be decreased nearly by two orders of magnitude to get that precision. The computational time required for every time step is essentially the same for both schemes and this has been the main motivation to use the fourth order scheme in our computations. Nevertheless, AB4BD4 requires a bit more memory storage and this factor must be considered by the user.

As mentioned in the introduction, one of the novelties of the presented method is the use of half Gauss–Lobatto grid in the radial coordinate. The use of standard mappings, $x = 2r - 1$, identifying the radial domain $r \in [0, 1]$ with the Cartesian interval $x \in [-1, 1]$ is a common practice in spectral methods in cylindrical coordinates [14,15,19,22]. The clustering of quadrature points near the wall, i.e., $r = 1$ or $x = +1$ is justified by the presence of boundary layers and strong gradients of the physical variables in that region, being necessary to resolve the physical phenomena within those small scales. However, the accumulation of radial points near the center axis has no physical justification unless remarkable variations of the flow speed take place in a neighbourhood of the pole. This is not the case in the Hagen–Poiseuille problem, where the axial profile is smooth and exhibits a maximum at $r = 0$.

Wherever semi-implicit time marching schemes are used, the time step size $\Delta t$ is conditioned by the *advective time scale*, $\tau_{\max} = dh/c_{\max}$, where $d$ is a typical length scale of the problem, $c_{\max}$ is the advection speed and $h$ is the grid size [3]. A straightforward geometrical analysis of the radial-azimuthal clustering in a standard collocation scheme $x = 2r - 1$ leads to

$$h \sim \frac{1}{M^2 N}, \tag{75}$$

where $M$ is the number of radial points, clustered near the origin via the asymptotic behaviour of the Gauss–Lobatto distribution, $1 - \cos(\pi/M) \sim \pi^2/2M^2$, and $N$ is the number of azimuthal points, leading to an arclength clustering

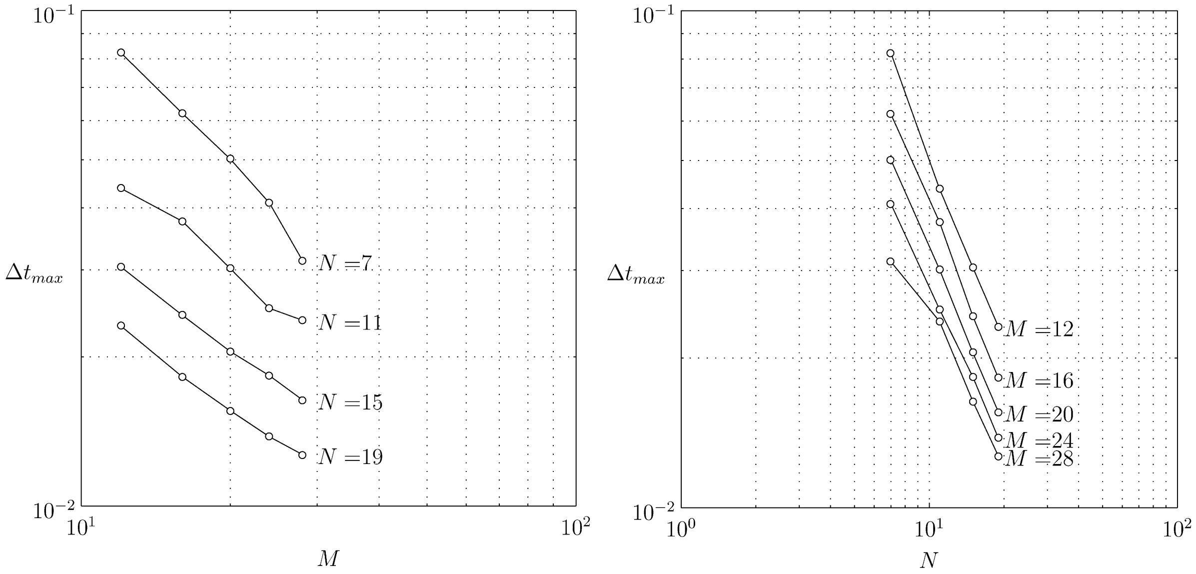

Fig. 9. $\Delta t_{\max}$ as a function of the number of radial and azimuthal modes.

proportional to $N^{-1}$. Provided that the order of maximum speed of the flow is $\mathrm{O}(c_{\max}) \sim 1$ and the typical length of the problem is the nondimensional pipe radius, $\mathrm{O}(d) = 1$, the advective restriction (75) leads to $\tau_{\max} \sim \mathrm{O}(N^{-1}M^{-2})$, whereas the asymptotic radial clustering given by (39) provides a milder accumulation ratio near the pole

$$r^{+}_{(M+3)/2} - r^{+}_{(M+1)/2} = -\cos\left(\frac{\pi(M+1)}{2M}\right) \sim \frac{\pi}{2M}, \tag{76}$$

leading to a less restrictive limit $\tau_{\max} \sim \mathrm{O}(N^{-1}M^{-1})$. The dependence $\Delta t_{\max}(N, M)$ has been explored within the range $(N, M) \in [7, 19] \times [12, 28]$, for $Re = 2500$ and a total time of integration $T = 100$, starting with the same initial condition prescribed in (72). The maximum time step $\Delta t_{\max}$ has been plotted against $M$ and $N$ in Fig. 9. The behaviour of $\Delta t_{\max}(N)$ for fixed $M$ is the same as in other integration schemes (Fig. 9, right), whereas a remarkable improvement can be observed in Fig. 9, on the left, where $\Delta t_{\max}(M)$ for fixed $N$ has been represented. Only two-dimensional perturbations have been included at $t = 0$, thus reducing the exploration to streamwise-independent dynamics. Although we have just focused our analysis on the radial-azimuthal clustering effect, the density of points in the axial coordinate will also affect the maximum time step size, the limitations being the same as in any other equispaced spectral scheme.

## 8. Transition to turbulence

This section is devoted to a performance analysis of the presented numerical solver in capturing the essential features of transitional pipe turbulence. The study of fully developed turbulence is out of the scope of the present work.

As mentioned in previous section, two-dimensional streaks might be destabilized by three-dimensional infinitesimal disturbances. This mechanism is just one possible scenario of transition to turbulence in shear flows and it is usually referred to as *streak breakdown* [16,21,23,26]. In order to obtain a *streak breakdown*, three-dimensional disturbances of a suitable axial periodicity must be added to the two-dimensional perturbation. The new initial condition is:

$$\mathbf{u}^0_{\mathrm{S}} = \mathbf{u}^0_{\mathrm{2D}} + \mathbf{u}^0_{\mathrm{3D}}, \tag{77}$$

where $\mathbf{u}^0_{\mathrm{2D}}$ is the same perturbation described in (72), and $\mathbf{u}^0_{\mathrm{3D}}$ is a three-dimensional disturbance of the form

$$\mathbf{u}^0_{\mathrm{3D}} = \sum_{l=5,6,7} \sum_{n=0,1} \mathrm{A}^{ln}_{\mathrm{3D}} \mathbf{v}_{ln} + \text{c.c.}, \tag{78}$$

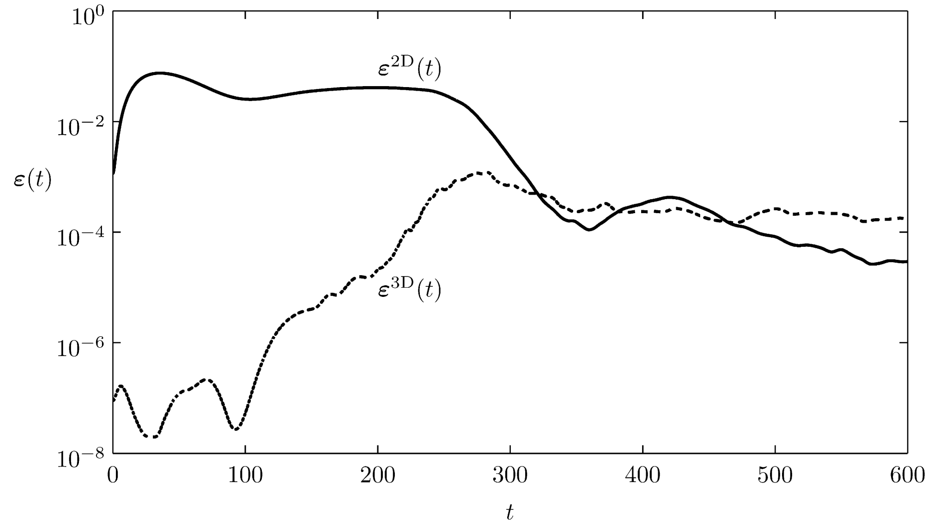

Fig. 10. Energies $\boldsymbol{\varepsilon}^{2\mathrm{D}}(t)$ and $\boldsymbol{\varepsilon}^{3\mathrm{D}}(t)$ as a function of time, exhibiting the *streak breakdown* mechanism of transition to turbulence.

where the fields $\mathbf{v}_{ln}$ are

$$\mathbf{v}_{ln} = \begin{cases} \mathrm{e}^{\mathrm{i}\mathrm{k}_0 l z}(0, f_3(r), 0) & (n = 0), \\ \mathrm{e}^{\mathrm{i}(\mathrm{k}_0 l z + n\theta)}(-\mathrm{i} n f_1(r), f_2(r), 0) & (n = 1), \end{cases} \tag{79}$$

with $f_3(r) = r(1 - r^2)$. In this case, $\mathrm{k}_0$ must be suitably chosen so an optimal range of axial wave numbers $\mathrm{k}_l = l\mathrm{k}_0$ are initially activated. In previous works [16,26], it has been proved that the optimal range of axial periodicities depends on the initial amplitude of the two-dimensional perturbation and the Reynolds number. A comprehensive exploration is not the aim of this analysis, so a particular case has been considered to test fully three-dimensional unsteady transitional dynamics. In particular, some axial wave numbers within the range $\mathrm{k} \in [1.5, 2.2]$ have been excited at $t = 0$. As in previous section, the bulk of the initial energy is mainly assigned to the two-dimensional component of the perturbation so that $\boldsymbol{\varepsilon}_0^{2\mathrm{D}} \sim 10^{-3}$, whereas the amplitudes $\mathrm{A}_{3\mathrm{D}}^{ln}$, for $n = 0, \pm 1$ and $\mathrm{k}_{\pm 5, \pm 6, \pm 7} = 1.5625, 1.875, 2.1875$, are uniformly activated leading to a much smaller total three-dimensional energy $\boldsymbol{\varepsilon}_0^{3\mathrm{D}} \sim 1 \times 10^{-7}$. This is accomplished by choosing $\mathrm{k}_0 = 0.3125$ and $L = 16$, so that medium-long wavelengths dynamics are also captured, leading to a pipe length $Q = 2\pi/\mathrm{k}_0 \sim 20$. Overall, the computations reported here have been carried out with $L = 16$, $N = 16$ and $M = 32$, equivalent to a $M_r \times N_\theta \times L_z = 33 \times 33 \times 33$-radial × azimuthal × axial grid. The fixed length of the pipe and the number of axial modes fix the maximum axial wavenumber to $\mathrm{k}_{\max} = 5.0$. It is well known that high axial-azimuthal frequencies require a considerable number of radial modes to be resolved [20]. Nevertheless, transitional dynamics are strongly dominated by low or medium axial wavenumbers, the high frequencies being only important once fully developed turbulence has been established.

For $Re = 5012$, Fig. 10 shows a typical example of the evolution of the energies $\boldsymbol{\varepsilon}^{2\mathrm{D}}(t)$ and $\boldsymbol{\varepsilon}^{3\mathrm{D}}(t) = \boldsymbol{\varepsilon}(\mathbf{u}_{3\mathrm{D}}(t))$ associated with the two-dimensional and three-dimensional perturbations, respectively. The sudden exponential growth of $\boldsymbol{\varepsilon}^{3\mathrm{D}}(t)$ is due to the inviscid instability. The computation shown in Fig. 10 covered $T = 600$ nondimensional time units, with a time step $\Delta t = 10^{-3}$ and using the AB4BD4 scheme. The nearly $6 \times 10^5$ time steps required about 80 hours on a 3.0 GHz AMD Athlon CPU.

## 9. Conclusions

A solenoidal spectral Petrov–Galerkin formulation for the spatial discretization of incompressible Navier–Stokes equations in unbounded cylindrical geometries has been formulated and implemented within a high order linearly implicit time marching scheme. The spatial discretization identically satisfies the incompressibility condition and the pressure terms are eliminated in the projection. The solenoidal fields satisfy suitable regularity conditions at the pole and radial clustering is avoided by using half Gauss–Lobatto meshpoints and modified Chebyshev polynomials of selected parity, thus allowing fast transform in the radial coordinate. The resulting radial-azimuthal mesh leads to less restrictive explicit time marching conditions. For the efficient evaluation of the nonlinear term, dealiased partial summation techniques have been formulated. The spatial discretization has been proven to converge spectrally in all linear cases studied. For unsteady nonlinear computations, modified $\mathrm{AB}_2\mathrm{BD}_2$ and $\mathrm{AB}_4\mathrm{BD}_4$ linearly implicit schemes have been used, the last proven to be more convenient for this particular problem. Different spatio-temporal convergence analysis have been provided and the time evolution of streamwise vortices has been studied as a test case. Streamwise streaks have been computed and their structure and energy distribution is almost identical to the ones formerly computed by other authors using different discretization schemes. Transitional dynamics to turbulence has been computed by means of the usually termed streak breakdown scenario, and the streamwise dependent modes that destabilize the streaks have axial periodicities within the interval predicted by former studies.

## References

[1] G.K. Batchelor, An Introduction to Fluid Dynamics, Cambridge University Press, Cambridge, 1967.

[2] L. Boberg, U. Brosa, Onset of turbulence in a pipe, Z. Naturforsch. A: Phys. Sci. 43 (1988) 697–726.

[3] J.P. Boyd, Chebyshev and Fourier Spectral Methods, Dover, New York, 1999.

[4] C. Canuto, M.Y. Hussaini, A. Quarteroni, T.A. Zang, Spectral Methods in Fluid Dynamics, Springer-Verlag, Berlin, 1988.

[5] S.M. Cox, P.C. Matthews, Exponential time differencing for stiff systems, J. Comp. Phys. 176 (2002) 430–455.

[6] P.G. Drazin, Introduction to Hydrodynamic Stability, Cambridge University Press, Cambridge, 2002.

[7] P.G. Drazin, W.H. Reid, Hydrodynamic Stability, Cambridge University Press, Cambridge, 1981.

[8] B. Fornberg, A Practical Guide for Pseudospectral Methods, Cambridge University Press, Cambridge, 1996.

[9] E. Hairer, G. Wanner, Solving Ordinary Differential Equations II: Stiff and Differential-Algebraic Problems, Springer-Verlag, Berlin, 1991.

[10] A. Iserles, A First Course in the Numerical Analysis of Differential Equations, Cambridge University Press, Cambridge, 1996.

[11] J. Komminaho, Direct Numerical Simulation of Turbulent Flow in Plane and Cylindrical Geometries, PhD Thesis, Royal Institute of Technology, Stockholm, 2000.

[12] M.T. Landahl, A note on an algebraic instability of inviscid parallel shear flows, J. Fluid Mech. 98 (1980) 243–251.

[13] A. Leonard, W. Reynolds, Turbulent research by numerical simulation, in: D. Coles (Ed.), Perspectives in Fluid Mechanics, Springer-Verlag, New York, 1988, pp. 113–142.

[14] A. Leonard, A. Wray, A new numerical method for the simulation of three dimensional flow in a pipe, in: E. Krause (Ed.), Proceedings of the 8th Int. Conf. on Numerical Methods in Fluid Dynamics, Springer-Verlag, Berlin, 1982, pp. 335–342.

[15] N. Mac Giolla Mhuiris, Calculations of the stability of some axisymmetric flows proposed as a model of vortex breakdown, App. Num. Math. 2 (1986) 273–290.

[16] A. Meseguer, Streak breakdown instability in pipe Poiseuille flow, Phys. Fluids 5 (15) (2003) 1203–1213.

[17] A. Meseguer, L.N. Trefethen, A spectral Petrov–Galerkin formulation for pipe flow I: Linear stability and transient growth, Oxford University, Numerical Analysis Group, Tech. Rep. 00/18, Oxford, 2000.

[18] A. Meseguer, L.N. Trefethen, Linearized pipe flow to Reynolds number $10^7$, J. Comp. Phys. 186 (2003) 178–197.

[19] P.L. O'Sullivan, K.S. Breuer, Transient growth in circular pipe flow. II. Nonlinear development, Phys. Fluids 6 (11) (1994) 3652–3664.

[20] V.G. Priymak, T. Miyazaki, Accurate Navier–Stokes investigation of transitional and turbulent flows in a circular pipe, J. Comp. Phys. 142 (1998) 370–411.

[21] S.C. Reddy, P.J. Schmid, J.S. Baggett, D.S. Henningson, On stability of streamwise streaks and transition thresholds in plane channel flows, J. Fluid Mech. 365 (1998) 269–303.

[22] P.J. Schmid, D.S. Henningson, Optimal energy growth in Hagen–Poiseuille flow, J. Fluid Mech. 277 (1994) 197–225.

[23] P.J. Schmid, D.S. Henningson, Stability and Transition in Shear Flows, Springer-Verlag, New York, 2001.

[24] H. Shan, B. Ma, Z. Zhang, F.T.M. Nieuwstadt, Direct numerical simulation of a puff and slug in transitional cylindrical pipe flow, J. Fluid Mech. 389 (1999) 39–60.

[25] L.N. Trefethen, Spectral Methods in MATLAB, SIAM, Philadelphia, PA, 2000.

[26] O.Y. Zikanov, On the instability of pipe Poiseuille flow, Phys. Fluids 8 (11) (1996) 2923–2932.